ORNL/TM-11254

ornl

OAK RIDGE
NATIONAL
LABORATORY

MARTIN MARIETTA

OAK RIDGE NATIONAL LABORATORY
CENTRAL RESEARCH LIBRARY
CIRCULATION SECTION
4500N ROOM 175
LIBRARY LOAN COPY
DO NOT TRANSFER TO ANOTHER PERSON
If you wish someone else to see this report, send in name with report and the library will arrange a loan.

ATF-II Studies

J. F. Lyon
B. A. Carreras
N. Dominguez
L. Dresner
C. L. Hedrick
S. P. Hirshman
M. S. Lubell
J. W. Lue
R. N. Morris
S. L. Painter
J. A. Rome
W. I. van Rij

OPERATED BY
MARTIN MARIETTA ENERGY SYSTEMS, INC.
FOR THE UNITED STATES
DEPARTMENT OF ENERGY

This report has been reproduced directly from the best available copy.

Available to DOE and DOE contractors from the Office of Scientific and Technical Information, P.O. Box 62, Oak Ridge, TN 37831; prices available from (615) 576-8401, FTS 626-8401.

Available to the public from the National Technical Information Service, U.S. Department of Commerce, 5285 Port Royal Rd., Springfield, VA 22161.
NTIS price codes—Printed Copy: A03 Microfiche A01

This report was prepared as an account of work sponsored by an agency of the United States Government. Neither the United States Government nor any agency thereof, nor any of their employees, makes any warranty, express or implied, or assumes any legal liability or responsibility for the accuracy, completeness, or usefulness of any information, apparatus, product, or process disclosed, or represents that its use would not infringe privately owned rights. Reference herein to any specific commercial product, process, or service by trade name, trademark, manufacturer, or otherwise, does not necessarily constitute or imply its endorsement, recommendation, or favoring by the United States Government or any agency thereof. The views and opinions of authors expressed herein do not necessarily state or reflect those of the United States Government or any agency thereof.

ORNL/TM-11254
Dist. Category UC-426

Fusion Energy Division

ATF-II STUDIES

J. F. Lyon
B. A. Carreras
N. Dominguez
L. Dresner
C. L. Hedrick
S. P. Hirshman
M. S. Lubell
J. W. Lue
R. N. Morris*
S. L. Painter
J. A. Rome
W. I. van Rij*

*Computing and Telecomunications Division, Martin Marietta Energy Systems, Inc.

Date published: October 1989

Prepared for the
Office of Fusion Energy
Budget Activity No. AT 10

Prepared by the
OAK RIDGE NATIONAL LABORATORY
Oak Ridge, Tennessee 37831-6285
operated by
MARTIN MARIETTA ENERGY SYSTEMS, INC.
for the
U. S. Department of Energy
under contract DE-AC05-84OR21400

MARTIN MARIETTA ENERGY SYSTEMS LIBRARIES

3 4456 0328277 5

CONTENTS

ACKNOWLEDGMENTS iv
ABSTRACT v
I. INTRODUCTION 1
II. LOW-ASPECT-RATIO PHYSICS ISSUES 3
II.A Magnetic Surface Fragility 3
II.B MHD Equilibrium and Stability Beta Limits 3
II.C Pressure-Driven Currents 3
II.D Energetic Orbit Confinement 4
II.E Low-Collisionality Transport 5
II.F Anomalous Edge Transport 5
III. COMPACT TORSATRON APPROACH 5
IV. INITIAL RESULTS OF INTEGRATED OPTIMIZATION STUDIES 9
V. A REFERENCE ATF-II CASE 14
VI. PERFORMANCE PROJECTIONS 18
VII. CONCLUSIONS 20
APPENDICES
A. INTEGRATED OPTIMIZATION STUDIES 21
B. SUPERCONDUCTING WINDIGN OPTIMIZATION 22
REFERENCES 27

ACKNOWLEDGMENTS

The authors acknowledge useful discussions with J. N. Luton, V. E. Lynch, and B. E. Nelson of Oak Ridge National Laboratory and with I. N. Sviatoslavsky of the University of Wisconsin and the encouragement of J. Sheffield, L. A. Berry, O. B. Morgan, and M. W. Rosenthal of Oak Ridge National Laboratory.

ABSTRACT

Design studies for a low-aspect-ratio, large next-generation stellarator, ATF-II, with high-current-density, high-field, stable NbTi/Cu helical windings are described. The design parameters are an average plasma radius of 0.52 m, a major radius of 2 m, and a field on axis of 4–5 T, with 10 to 15 MW of heating power. Such a device would be comparable in scope to other next-generation stellarators but would have roughly the same aspect ratio as the tokamaks without, however, the need for current drive to sustain steady-state operation. A number of low-aspect-ratio physics issues need to be addressed in the design of ATF-II, primarily compromises between high-beta capability and good confinement properties. A six-field-period Compact Torsatron is chosen as a reference design for ATF-II, and its main features and performance predictions are discussed. An integrated (beta capability and confinement) optimization approach and optimization of superconducting windings are also discussed.

I. INTRODUCTION

The primary goal of ATF-II, a potential successor to the existing Advanced Toroidal Facility (ATF), is to study some of the key issues relating to the feasibility of stellarators as attractive steady-state reactors. This goal is similar to that of the other large next-generation stellarators[1,2] now under design, the Large Helical Device[3] (LHD) and Wendelstein VII-X[4] (W VII-X), but ATF-II would follow a low-aspect-ratio approach, similar to that of the mainstream tokamaks. A major motivation for adopting this approach[5] is to reduce the cost of the stellarator deuterium-tritium (D-T) demonstration step that would follow a successful next-generation hydrogen plasma experiment. The specific issues that ATF-II should address are high-beta, steady-state operation; confinement at low collisionality; loss of energetic helically trapped particles; particle and impurity control; plasma heating and heat removal; endurance of wall materials and in-vessel components; and integration of superconducting coils in a working experiment.

Some of these issues can be partially addressed in ATF,[6] but most of them will require the higher plasma parameters and steady-state capability at higher power that make ATF-II a significant step beyond ATF. Larger average plasma radius ($\bar{a} \simeq 0.5$ m) is needed to reduce the effect of edge-dominated losses and to increase the energy confinement time ($\tau_E \propto \bar{a}^2$, from Ref. 7). The low aspect ratio $A = R_0/\bar{a} = 3$–5 assumed for ATF-II leads to a major radius similar to that of ATF ($R_0 = 2.1$ m), which also lowers the cost ($\propto R_0^{2.1}$, from Ref. 8) and maximizes compatibility with the present ATF site. A higher magnetic field ($B = 4$ T) is needed to improve confinement (energy confinement time $\tau_E \propto B_0^{0.84}$, from Ref. 7) and to allow use of electron cyclotron heating (ECH) for current-free operation, radial electric field control, and electron heating at plasma densities near 10^{20} m^{-3}; the ordinary-mode (O-mode) cutoff density is $\simeq 1.5 \times 10^{20}$ m^{-3} for the 112-GHz electron cyclotron resonance at 4 T. Higher plasma heating power ($P = 10$–15 MW) is needed to make definitive tests of beta limits, low-collisionality transport, impurity control, and edge power handling at higher plasma parameters. Superconducting coils are needed for steady-state operation at maximum field to study the plasma-wall equilibration, to study the long-term evolution of high-beta plasmas at lower field (for times much longer than the skin diffusion time scale), and to avoid the high power consumption of copper coils [$\simeq$340 MW for an $M = 6$ (here M is the number of field periods) ATF-II with $R_0 = 2$ m and $B_0 = 4$ T]. Hydrogen plasma operation is chosen to avoid the problems (and cost) associated with neutron shielding, activation, and remote handling.

Figure 1 compares the plasma radius, major radius, and magnetic field of proposed next-generation stellarators (open circles) to those of present-day stellarators (solid circles) and tokamaks (solid squares). The dashed lines are lines of constant A. ATF-II would be a substantial advance in size, field, and heating power over present-day stellarators and would have device parameters between those of some earlier tokamaks that achieved high plasma performance [e.g., the Princeton Large Torus (PLT) and ASDEX] and those of some of the newer generation of larger tokamaks (ASDEX-Upgrade and the tokamaks with superconducting toroidal field coils, Tore Supra and T-15). ATF-II would have roughly the same plasma radius

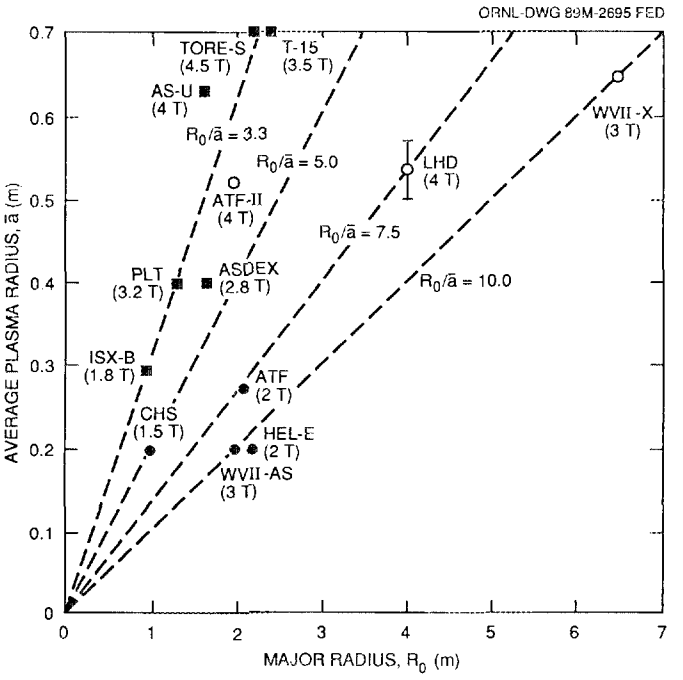

Fig. 1. Relationship of ATF-II to other toroidal experiments: present-day stellarators (CHS, W VII-AS, Heliotron E, ATF), represented by solid circles; some older tokamaks (ISX-B, PLT, ASDEX) and some newer tokamaks (Tore Supra, T-15, and ASDEX-Upgrade), represented by solid squares; and the other next-generation stellarators (LHD, W VII-X).

as LHD and W VII-X and roughly the same plasma aspect ratio as tokamaks, but without the tokamaks' need for current drive to sustain steady-state operation.

The main constraints placed on the ATF-II design studies described here are low aspect ratio ($A = 3$–5), device cost [$\simeq$\$50 million to \$100 million on the device-only cost basis that yields a cost of \$20 million for ATF (power supplies, heating, controls, diagnostics, utilities, etc., extra)], and steady-state capability at 4 T. These studies are still in the design scoping stage and have not yet resulted in a final concept for ATF-II. The goal of these studies is to find a magnetic configuration for ATF-II with magnetohydrodynamic (MHD) and confinement properties at least as good as those projected for ATF,[6] at approximately half the plasma aspect ratio of ATF, that can be realized with a coil configuration that is attractive for a next-generation experiment and for extrapolation to a reactor. Two main approaches are still being explored: an ATF-II based on a particular helical winding trajectory, the Compact Torsatron,[9] which we take as the reference design because it is more developed, and an ATF-II based on a specified shape for the plasma boundary that gives the desired plasma properties.

This paper discusses general low-aspect-ratio physics issues, results from the two design optimization approaches used, a particular reference design for ATF-II, and some performance projections. An integrated MHD and confinement optimization approach is described in Appendix A, and superconducting winding optimization studies are described in Appendix B.

II. LOW-ASPECT-RATIO PHYSICS ISSUES

A number of physics issues relating to finite-beta behavior and transport are important in optimization of low-aspect-ratio configurations.[10] The most important finite-beta issues are fragility of magnetic surfaces, MHD equilibrium and stability beta limits, and pressure-driven (bootstrap) currents. Transport issues include energetic orbit confinement, transport at low collisionality, and anomalous edge transport.

II.A. Magnetic Surface Fragility

At low aspect ratio, the $1/R$ helical-symmetry-breaking terms in the magnetic field expansion become more important. In the vacuum configuration, they result in the destruction of the outer magnetic surfaces. This effect has been taken into account in the Compact Torsatron studies by using the Cary-Hanson technique[11] to restore the broken outer magnetic surfaces. At finite beta, the beta-induced outward magnetic axis shift increases the magnitude of the helical-symmetry-breaking terms such that they can severely limit the achievable beta. The solution[9] to this problem proposed for ATF-II is the use of an axisymmetric poloidal field [vertical field (VF)] coil system with active feedback to control the magnetic surfaces as beta increases.

II.B. MHD Equilibrium and Stability Beta Limits

The beta limit is the lower of the limits set by MHD equilibrium and stability. In general, stability is not an issue at low aspect ratio, unless the magnetic configuration is modified substantially to improve confinement. For low-aspect-ratio torsatrons, such as ATF and the Compact Helical System (CHS), the main stabilization mechanisms are the magnetic well at the plasma center and the shear at the plasma edge.[9] This combination produces a beta self-stabilization effect,[12] arising from the β^2 term in the Mercier stability criterion,[13] that leads to a high-beta second stability regime. As shown in Fig. 2, the MHD stability limit for torsatrons increases with decreasing M (and A) until the beta limit is determined by an equilibrium beta limit, conventionally when the radially outward shift of the magnetic axis is half the plasma radius, related to $\beta_c = \iota^2(\bar{a})/A$, where ι is the rotational transform. For constant-pitch helical windings, $\iota(\bar{a}) \propto A$ as a result of the breaking of the outer magnetic surfaces, so $\beta_c \propto A$. Therefore, lower aspect ratio can lead to a lower equilibrium beta limit unless the edge value of ι can be prevented from decreasing. This is accomplished in Compact Torsatrons by poloidally modulating the helical winding trajectory [see Eq. (1) in Sec. III] such that $\iota(\bar{a}) \simeq 1$ and hence $\beta_c \propto 1/A$ increases, rather than decreases, with decreasing A.

II.C. Pressure-Driven Currents

Pressure-driven currents, in particular the bootstrap current, can be a problem for zero-net-current stellarator operation at low collisionality, independent of the

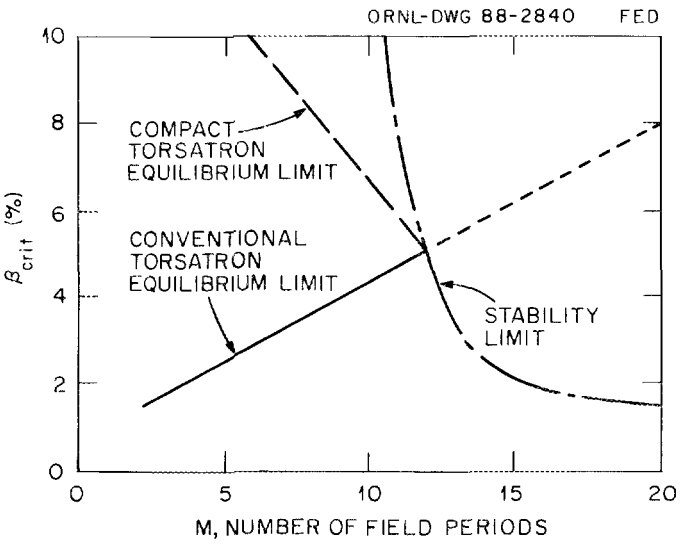

Fig. 2. The beta limit for Compact Torsatrons increases with decreasing M and A, rather than peaking at a moderate M value as does that for constant-pitch torsatrons.

aspect ratio, because plasma currents can modify the desired radial profile of ι, leading to instabilities. However, by using added magnetic field components (i.e., dipole or quadrupole components of the poloidal field) or by allowing a slight helical axis in the configuration, the bootstrap current can be reduced to essentially zero, as was shown in Ref. 14 for the ATF configuration. The poloidal field coil system for ATF-II would be designed to allow this reduction.

II.D. Energetic Orbit Confinement

Loss of energetic helically trapped particles can be large[15,16] in low-aspect-ratio torsatrons. For $A < 5$, essentially all the energetic helically trapped particles are lost down to energies of two to three times the thermal energy, below which the ambipolar radial electric field causes a poloidal orbit rotation that prevents the orbit loss. Heating mechanisms that utilize a fast-ion population with small $|v_{\parallel}/v|$, such as perpendicular neutral beam injection (NBI) or ion cyclotron heating (ICH), which creates a perpendicular high-energy distribution, would be the most susceptible to this loss. However, other energetic-particle heating mechanisms (e.g., tangential NBI) could also be affected because of the relatively rapid pitch-angle scattering of particles with energies below $E_{\rm crit}$ ($= 13.6T_e^{3/2}$ for protons in a hydrogen plasma). This is less of a problem in a reactor because alpha particles that are not directly lost must slow down substantially (from 3.5 MeV to ~0.4 MeV) before they pitch-angle scatter into the loss region at small $|v_{\parallel}/v|$. In any event, this power loss is less than that needed in a tokamak for current drive.

There are two ways to address this issue in ATF-II. The first is to use heating methods that do not utilize an energetic ion population: fundamental or

second harmonic ECH or fundamental ICH. Although fundamental ICH has been observed[17] at low power in the L-2 stellarator, a more substantial demonstration is needed before it could be relied upon to solve this problem in ATF-II. ECH has more experimental basis, and high-power (0.5- to 1-MW), high-frequency (110- to 140-GHz) gyrotrons are being developed that would satisfy the ATF-II requirement of operating in the 10^{20}-m^{-3} density range. In addition, normally oriented ECH does not introduce particles or momentum into the plasma, and the launching structures can be far from the plasma edge, thus minimizing the plasma-wall interaction and the impurity influx to the plasma. However, a better approach is to reduce the direct loss of energetic trapped particles by modifying the magnetic configuration properties. Quite large reductions in trapped particle losses can be obtained in this way for low-aspect-ratio configurations,[15] but these modifications can also affect the high-beta characteristics.

II.E. Low-Collisionality Transport

A major issue for stellarator confinement is neoclassical diffusive losses in the $1/\nu$ collisionality regime, where electric fields are not effective in improving confinement. The particle flux in the $1/\nu$ regime has been calculated in Ref. 18 for a multiple-helicity stellarator. When only toroidal ripple, $\epsilon_T = 1/A$, and helical ripple, ϵ_h, are considered, the particle flux scales as $\epsilon_h^{3/2}\epsilon_T^2 \propto 1/A^2$. Fortunately, the particle flux in a stellarator can be changed by changing the magnetic field structure; e.g., the calculated particle flux can be varied by more than a factor of five in ATF by varying the quadrupole component of the poloidal field.[10]

II.F. Anomalous Edge Transport

Present stellarators are dominated by anomalous electron transport in the outer part of the plasma. In ATF-II, anomalous edge transport may be reduced through the reduction of instability fluctuations (turbulence) in the second stability regime. Calculations of particle and heat diffusivity for pressure-gradient-driven turbulence[19] show that these transport coefficients are reduced in the second stability region. However, this has not yet been demonstrated experimentally, and we do not have a verified model for anomalous transport in stellarators. In fact, obtaining such an understanding is one of the objectives of the present generation of experiments (and extending this understanding at higher parameters is one of the objectives of ATF-II).

III. COMPACT TORSATRON APPROACH

Compact Torsatrons feature a helical winding trajectory characterized by

$$\phi = \phi_0 + \ell \left[\theta - \sum_n \alpha_n \sin(n\theta)\right]/M \ , \tag{1}$$

where ϕ and θ are the usual toroidal and poloidal angles and the multipolarity $\ell = 2$. The set of α_n values is chosen[9] to maximize $\iota(\bar{a})$ (using the Cary-Hanson

technique[11] of restoring broken outer flux surfaces) subject to the constraints of central rotational transform $\iota(0) \sim 0.3$ (to provide shear) and a central magnetic well $[V''(0) < 0$; the primes denote differentiation with respect to ψ (the toroidal flux) of the volume V within a flux surface$]$. The resulting Compact Torsatrons have $\iota(\bar{a}) \simeq 1$, high edge shear, and a magnetic well that usually extends to the $\iota = \frac{1}{2}$ surface. The nomenclature CTM is used to label a Compact Torsatron with M field periods. The main physics parameters for CT6, CT7, CT8, and CT9 are shown in Fig. 3. All have $A < 5$, and CT7 has $A \simeq 3.3$. In other respects, the configuration properties are similar to those of the moderate-aspect-ratio ATF ($A = 7.8$).

The primary advantages of the low-aspect-ratio Compact Torsatron approach over conventional torsatrons, in addition to lower cost, are the larger plasma volume and the greatly improved access between the helical windings, as illustrated in Fig. 4. As the number of field periods decreases from 12 to 6 in this Compact Torsatron sequence, the plasma and coil aspect ratios decrease by approximately a factor of

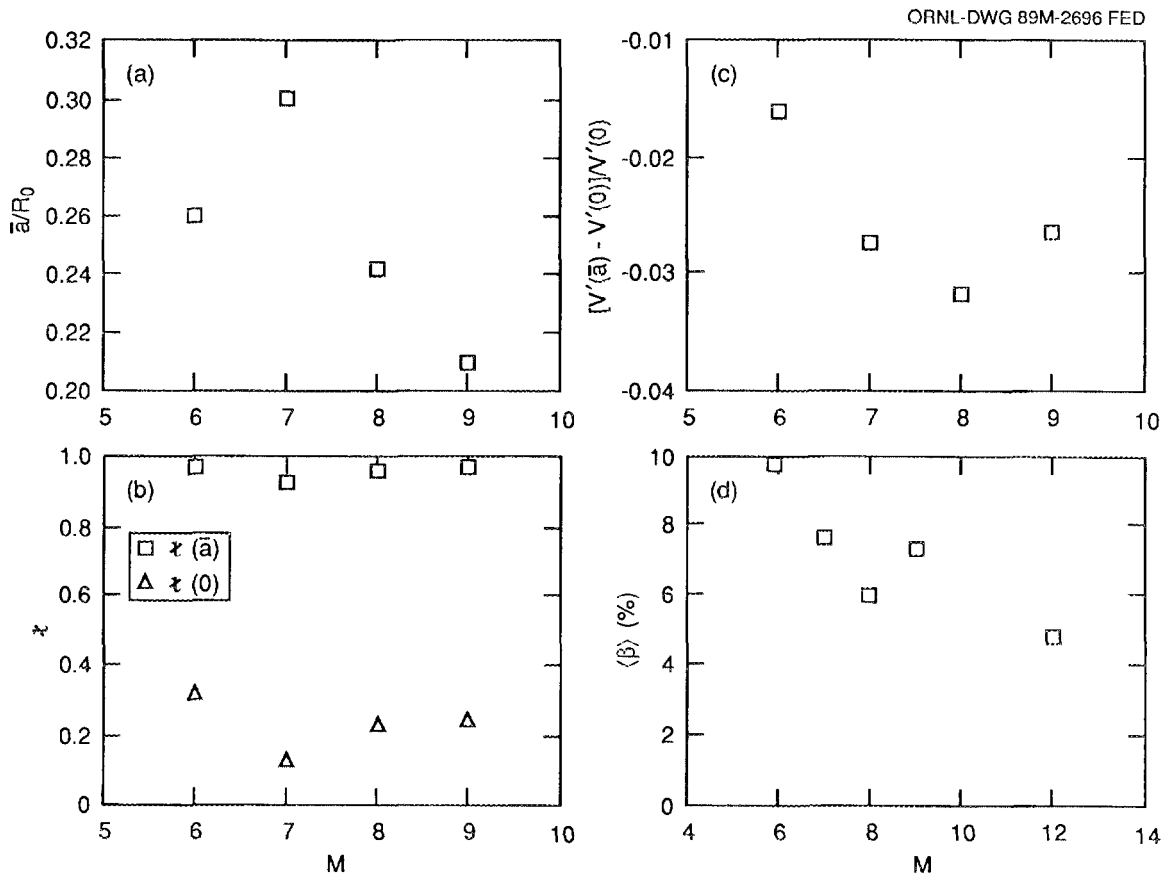

Fig. 3. Physics parameters for the Compact Torsatron sequence with $M = 6$ to 9: (a) inverse aspect ratio $\bar{a}/R_0$, (b) rotational transform ι, (c) magnetic well depth, and (d) calculated equilibrium beta limit.

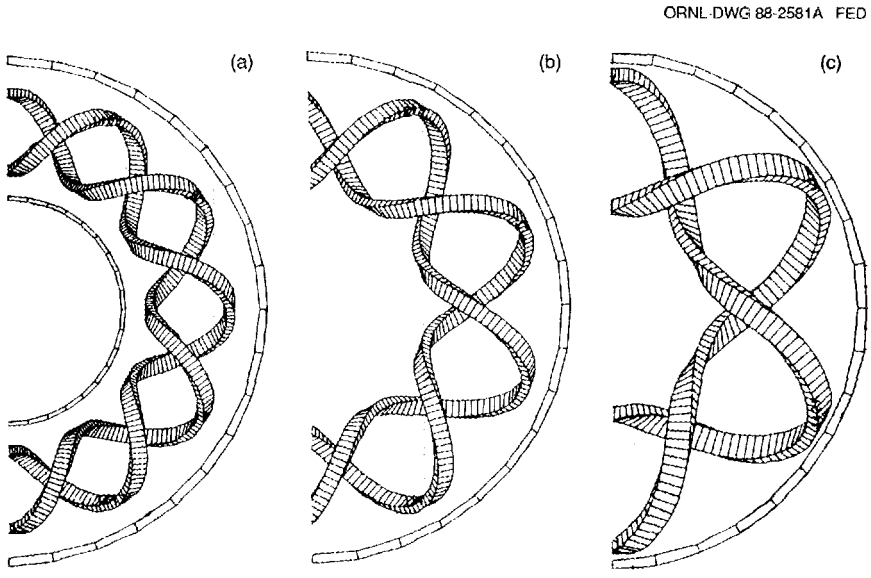

Fig. 4. Helical windings and VF coils for Compact Torsatrons with (a) $M = 12$, (b) $M = 9$, and (c) $M = 6$.

two, and the degree of access improves dramatically, especially on the outside and at the top and bottom. In an experiment, this improved access is important for plasma heating, pumping, and diagnostics. It is also important in a reactor because it provides more area for heat removal and the tritium breeding blanket, which lowers the required neutron multiplication in the blanket and simplifies maintenance.[20] Because the poloidal modulation of the helical winding pitch, the set of α_n values, changes as the number of field periods decreases in the Compact Torsatron sequence in order to keep the edge value of $\iota \simeq 1$, the access from the small-major-radius side decreases, but this is less important than the access elsewhere.

The standard Compact Torsatrons require only a single (outer) VF coil set to control the plasma position. However, additional VF coil sets would be provided at the inside and near the top and bottom (as on ATF, CHS, and LHD) to allow control of the bootstrap current, the variation of $\int dl/B$ on flux surfaces, etc., through control of $\iota(0)$ and the shaping of the magnetic surfaces. These coil sets are also useful in preventing breakup of the outer flux surfaces (ergodization) at finite beta. Figure 5 shows the approximate equivalence of changing the helical winding trajectory (choice of α_n values) and changing the currents in the VF coils for restoring broken magnetic surfaces.

Compact Torsatrons were optimized for their MHD properties and for low plasma aspect ratio. Analysis of energetic orbit confinement in these configurations indicates that a large fraction (typically half or more) of the energetic helically trapped ions would be lost; in a reactor, this is $\simeq$15–30% of the total energetic alpha-particle population.[15] While this loss is not serious for a reactor, it is important to reduce it in a next-generation experiment. In addition to this direct ion loss, there is a corresponding increase in the neoclassical electron thermal diffusivity.

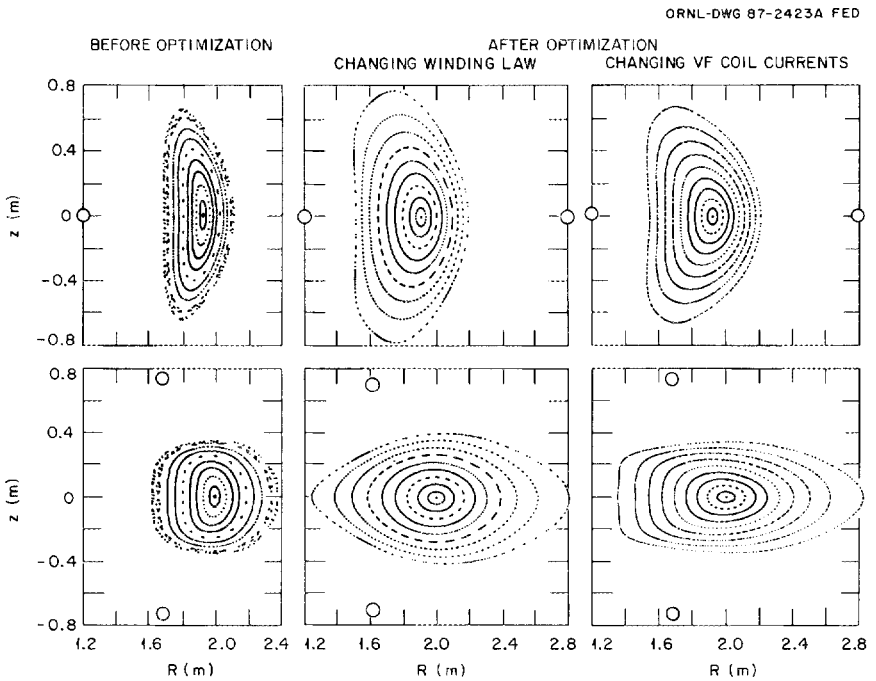

Fig. 5. Magnetic flux surfaces at the beginning (top) and halfway through a field period (bottom) before ($\alpha_n = 0$ for $n > 1$) and after optimization of the configuration.

A number of modifications can be made to the Compact Torsatron configurations to reduce the loss of energetic helically trapped particles in the vacuum magnetic configuration, such as shifting the magnetic axis inward, increasing the plasma ellipticity through the quadrupole component of the poloidal field,[10] and adding $\ell = 3$ components to the field which effectively cancel the finite-aspect-ratio $(1/R)$ component in the magnetic field expansion.[15] Large reductions in the direct energetic orbit losses (up to complete elimination of these losses) and in the electron thermal conductivity can be achieved in this way for the vacuum magnetic configuration. However, the confinement improvement quickly vanishes with increasing beta, and these modifications affect the MHD optimization. Figure 6 shows the increase in losses of helically trapped particles with increasing beta for ATF configurations [standard, shifted in, and with increased $\iota(0)$] and for the CT7 configuration with additional quadrupole field optimization. Modifying the poloidal field as beta increases may reduce the energetic particle losses for these vacuum-optimized configurations but may also change their beta limits. An integrated orbit and MHD optimization has not been done for the Compact Torsatron cases, so a completely satisfactory solution has not yet been found for a low-M ATF-II based on Compact Torsatrons. For concreteness, an $M = 6$ Compact Torsatron is chosen as the reference case for ATF-II, while an improved configuration is being sought through an integrated optimization approach.

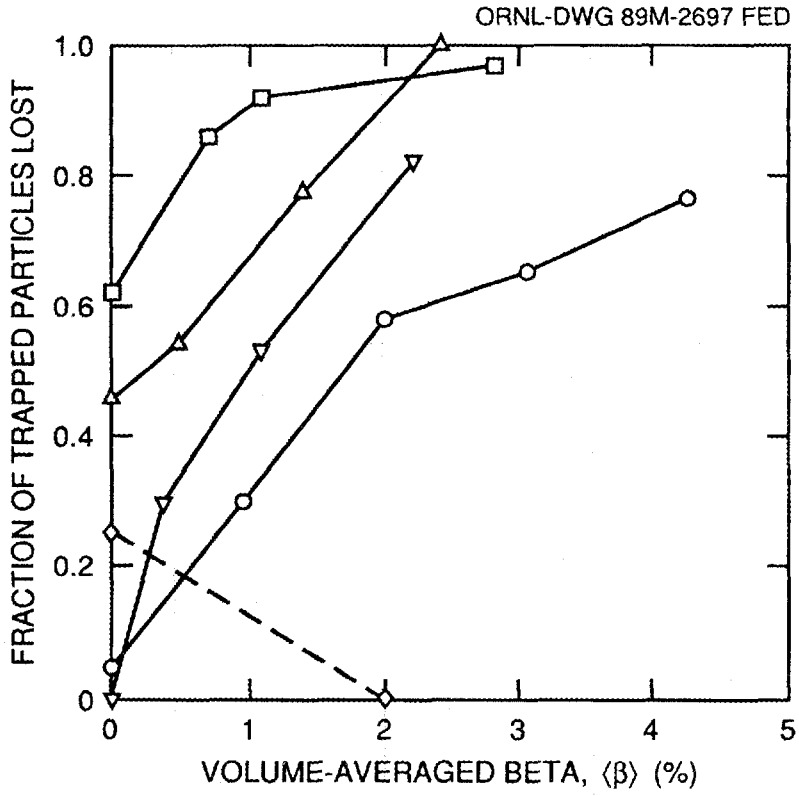

Fig. 6. The fraction of the energetic helically trapped ions that are lost rises rapidly with beta for ATF variants [standard configuration (Δ), shifted in (∇), and increased central transform ($\circ$)] and for an improved CT7 ($\square$) but remains at lower levels for an $A = 4$ integrated optimization case (dashed line).

IV. INITIAL RESULTS OF INTEGRATED OPTIMIZATION STUDIES

The integrated optimization approach is discussed in Appendix A. The optimization is done at finite beta with the fixed-boundary VMEC code. This approach is more fruitful than using an optimized vacuum (zero-beta) outer flux surface and then following it to higher beta, because there appears to be a much narrower range of desired configurations at higher beta; the finite-beta optimized configurations have good performance at zero beta, but the zero-beta optimized configurations may not perform as well at higher beta. The free-boundary VMEC code is used to calculate the changes in the magnetic configuration with beta.

Some initial results obtained with this approach, although preliminary, are encouraging and may lead to an ATF-II configuration with better energetic particle confinement than the Compact Torsatrons. Magnetic configurations with low aspect ratio, half that of ATF, that are Mercier stable and have confinement properties

similar to or better than those projected for ATF have been found. The results depend on the plasma pressure profile assumed. A peaked profile with weak edge gradients gives the best results. Most of the calculations used a pressure profile of the form $p(\psi) = p_0(1-\psi)^2(1-\psi^2)$. To obtain higher $\langle\beta\rangle$, it is desirable to flatten the pressure profile around the $\iota = \frac{1}{2}$ surface, where the plasma tends to become Mercier unstable.

Figure 7 shows the magnetic surfaces for an $A = 4$ configuration optimized at $\langle\beta\rangle = 2\%$ (Fig. 7a) and for the same configuration at zero beta (Fig. 7b). In Fig. 7a, a vertical field that centers the magnetic axis and optimizes alignment of the $B_{\min}$ contours with the flux surfaces has been applied. Without this vertical field, the magnetic axis would be shifted out radially by 20 cm, as shown in Fig. 7c. In addition to reducing the Shafranov shift, the applied vertical field reduces the depth and radial extent (from $\psi \simeq 0.65$ with no vertical field to $\psi \simeq 0.45$ with the vertical field) of the magnetic well. In spite of this erosion of the magnetic well, stability to Mercier modes is maintained throughout the plasma because the stabilizing contribution from the $\vec{j} \cdot \vec{B}$ term in the Mercier criterion increases and moves inward at the same rate that the well disappears. The stability of this configuration differs from that of Compact Torsatrons, which rely for high-beta stability on a magnetic well that deepens and expands radially with increasing beta. The vertical field causes a significant modification of the outer boundary shape, accounted for self-consistently by the free-boundary calculation, in addition to recentering the plasma. The Compact Torsatron optimization assumed that the plasma boundary was fixed as $\langle\beta\rangle$ increased, which is not a good assumption. The ι profile for this configuration is nearly identical to that of ATF, except for a slightly smaller edge transform (0.85 vs 1.0).

The fraction of energetic helically trapped particles that are lost is shown vs $\langle\beta\rangle$ by the dashed curve in Fig. 6. This configuration has considerably better

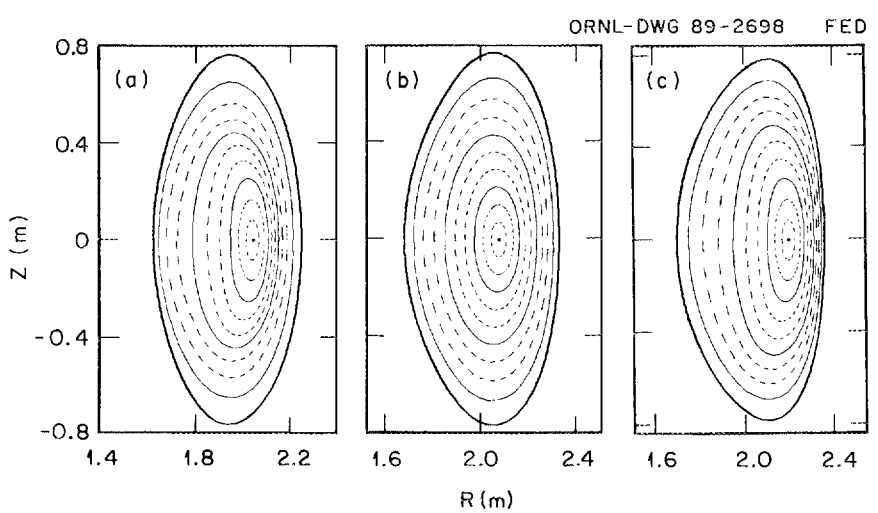

Fig. 7. Magnetic flux surfaces in the $\phi = 0$-deg plane for an $A = 4$ configuration (a) optimized at $\langle\beta\rangle = 2\%$, (b) at zero beta, and (c) at $\langle\beta\rangle = 2\%$ without an additional vertical field.

confinement at $\langle\beta\rangle \sim 2\%$ than either the ATF configuration variants or an improved CT7. We are investigating configurations that are Mercier stable at $\langle\beta\rangle = 5\%$, but more improvement is still needed in their high-beta confinement properties.

Some encouraging progress has been made on finding coil configurations[21] to create the magnetic configurations that result from the integrated optimization studies. The Garching NESCOIL code[22] is used to find a current distribution on an assumed surface that produces the last closed flux surface obtained from the integrated optimization procedure. Discrete current windings are then constructed from this current distribution. The finite-beta outer flux surface is treated as though it were a vacuum flux surface in generating the coils (the NESCOIL code assumes that there are no currents in the plasma). Stellarator configurations with continuous helical windings, modular coils, or combinations of the two can be created in this way. The complexity of the resulting winding geometry depends on the shape of the external surface on which the current distribution is calculated and on the distance of that surface from the plasma boundary. In general, simpler winding configurations are found when the external surface is closer to the plasma boundary and has the same shape as the boundary. There is a large degree of flexibility in the choice of the surface and the current distribution on the surface. Thus far, we have examined only surfaces that have the same shape as the plasma boundary.

The current distribution obtained on a surface 30 cm from the plasma boundary for a configuration optimized at $\langle\beta\rangle = 4\%$ is shown in Fig. 8. The helical features

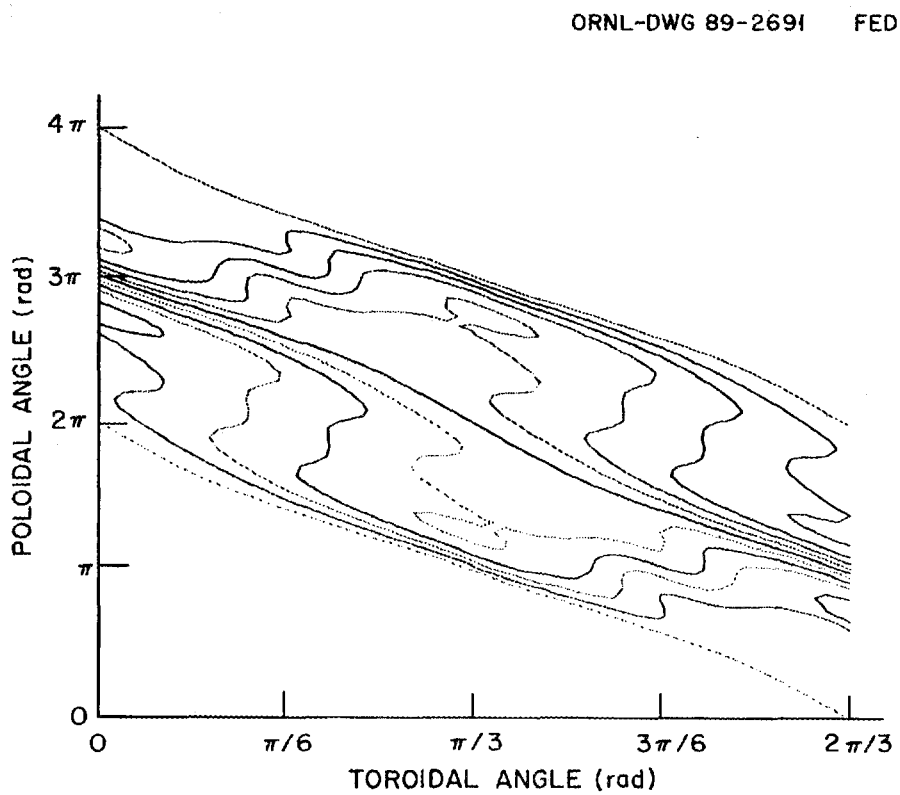

Fig. 8. Surface current distribution that creates an $A = 4$ configuration optimized at $\langle\beta\rangle = 4\%$.

in the current distribution suggest that at least part of it may be approximated by pieces of discrete helical coils. The resulting quasi-helical coil set is shown in Fig. 9. The single helical winding is only on the inside (small-R side); there is only one winding in each constant-ϕ cross section, but the pitch is the same as for $\ell = 2$. In a sense, this is an $\ell = 1.5$ configuration. The winding moves helically from the bottom to the top on the small-R side, changes to an oval planar coil at constant ϕ with half the current in the inside part of the oval coil and half in the outside part of the oval coil, and then continues helically from the bottom to the top again on the small-R side. This coil configuration provides even better access than the $\ell = 2$ Compact Torsatron windings. Modules containing the required additional (trim) modular coils and vacuum vessel segments can be inserted radially because there are no outside radial obstructions between the planar oval coils, which are spaced toroidally every 60 deg. However, much more work needs to be done with this coil configuration, especially with trim coils, to better approximate the surface current distribution in Fig. 8. It is premature to say whether this route will be successful.

Another approach is to use nonplanar modular coils with limited (but still large) toroidal excursions. The surface current distribution in Fig. 10 is for the same configuration and the same 30-cm plasma-coil spacing as in Fig. 8, but with no net toroidal current on the surface. This approach provides the freedom to add any current distribution on the surface that does not create a field inside that surface. A modular coil realization of the surface current distribution in Fig. 10 is shown in Fig. 11. This particular realization uses 10 coils per field period. The number of coils per period and the high-frequency spatial modulations seen in Fig. 11 could be relaxed.

ORNL-DWG 89-2692A FED

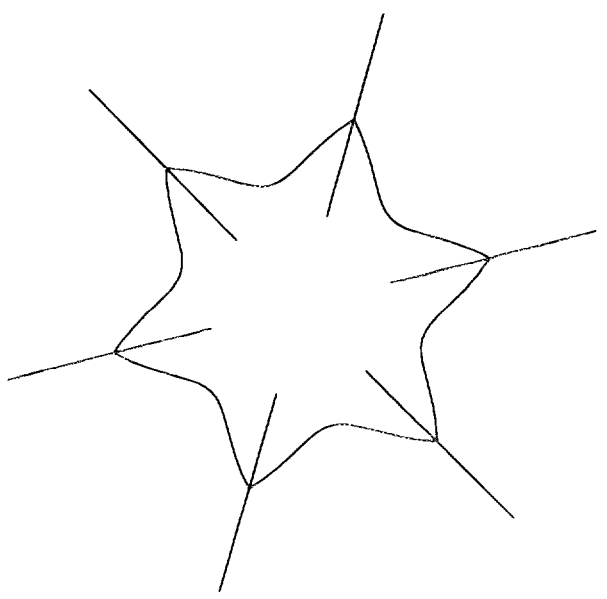

Fig. 9. Top view of the quasi-helical coil configuration that approximates the surface current distribution in Fig. 8.

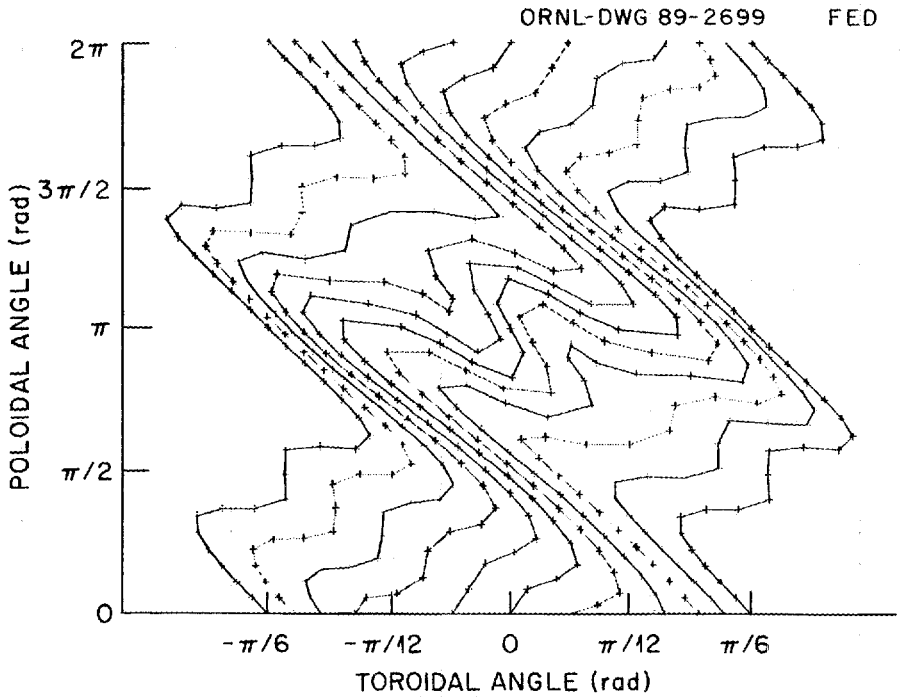

Fig. 10. Surface current distribution with no net toroidal current that creates an $A = 4$ configuration optimized at $\langle\beta\rangle = 4\%$.

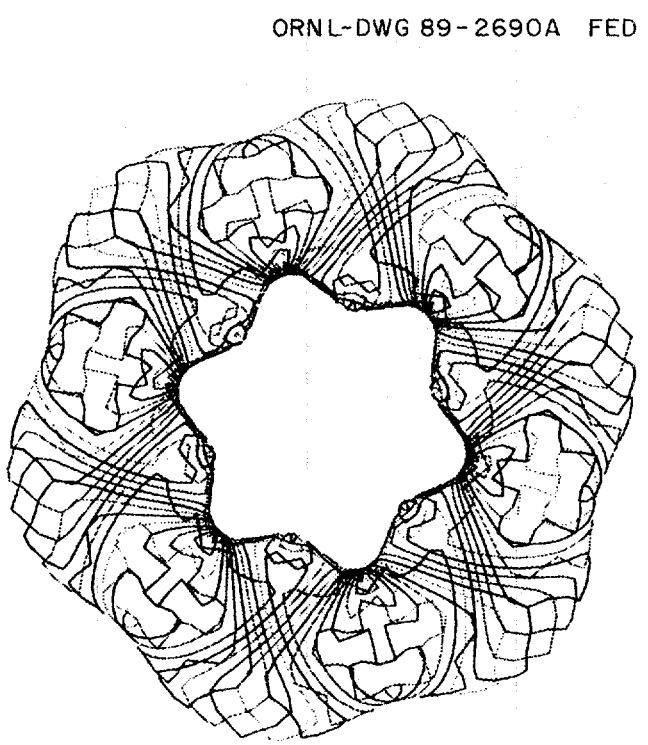

Fig. 11. Top view of the modular coil set that approximates the surface current distribution in Fig. 10.

The higher harmonic content (sharp bends, kinks, loops, etc.) of the surface current increases as the aspect ratio decreases or as the plasma-coil spacing increases. There is room to relax both of these constraints in our ATF-II studies, so we are hopeful that we can find a coil configuration that is attractive both from an engineering point of view (for good access in a low-aspect-ratio experiment or reactor) and from the physics point of view (good confinement at high beta).

V. A REFERENCE ATF-II CASE

The $M = 6$ Compact Torsatron CT6 has been chosen as the base reference case for the ATF-II studies. It has a low aspect ratio ($A = 3.9$), half that of ATF, and a rotational transform profile similar to that of ATF. It also extrapolates to an attractive reactor[20] with $R_0 \simeq 8$ m that has more than adequate beta (see Fig. 3d) and tolerable ripple-induced diffusive losses[20] and direct alpha-particle losses.[15] Figure 12 shows the two helical windings and the last closed flux surface for a CT6 ATF-II. The large access to the plasma on the outside, top, and bottom is evident. The helical windings are assumed to be NbTi conductor, wound on a precision helical (segmented) form that later becomes part of the structural case for the helical winding. A dewar is assumed to surround the helical windings. This

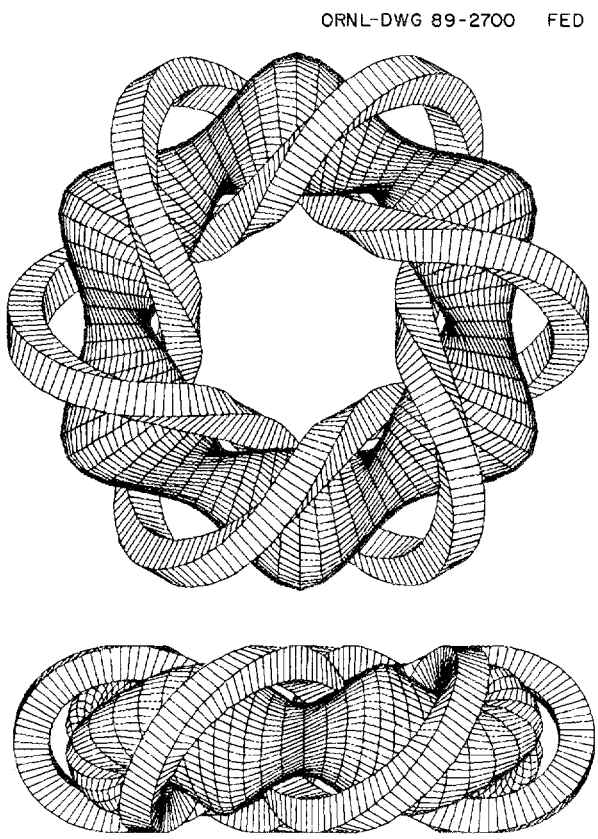

Fig. 12. The helical windings and the last closed flux surface for an $M = 6$ ATF-II.

construction allows a thin, replaceable, heated (for baking) or cooled (for steady-state operation) first wall between the plasma and the helical field (HF) and VF coil sets. The superconducting coil sets would be in a common doughnut-shaped vacuum vessel with vertical cylindrical side walls and curved top and bottom toroidal shells, similar to that proposed for LHD. An in-line, force-cooled, high-current power lead for the windings would be used to reduce refrigeration losses. Bellows would allow for the relative movements between the vacuum dewar, the helical windings, and the first wall that occur during warmup and cooldown of the helical windings and the first wall.

Steady-state operation of ATF-II introduces constraints that are more restrictive than for short-pulse (3- to 10-s) experiments. In short-pulse experiments, the wall can pump particles (e.g., with gettered surfaces), and in-vessel components (wall, antennas, etc.) can cool down between pulses (no active cooling required). The absence of these transitory effects means that adequate interior space and vacuum vessel access must be provided for replaceable cooled wall panels and for continuous pumping of either the scrape-off layer or the divertor stripe. The use of superconducting windings dictates an inner-vacuum first wall so that access to the plasma region does not require warming up the HF and VF coils.

The choice of the principal parameters ($B_0 = 4$ T, $R_0 \simeq 2$ m) for ATF-II is determined by various constraints: geometry, the maximum field on the superconductor, and cost. The need for adequate space between the plasma edge and the vacuum wall is a major factor in determining the allowable values of B_0 and R_0 for ATF-II and other next-generation stellarators. The total distance from the plasma edge (the last closed flux surface) to the center of the helical winding is given by $\Delta = x_{\rm pw} + x_{\rm m} + c = R_0/A_\Delta$. Here $x_{\rm m}$ is the combined thicknesses of the first wall, the assembly gap, the cryostat, and the coil case; $x_{\rm pw}$ is the minimum plasma-wall separation; c is the half-radial depth of the helical winding; and A_Δ is a geometrical constant for a given configuration; e.g., for CT6, $A_\Delta = 6.62$. We set $x_{\rm pw} = 15$ cm; the thin diverted flux layer outside the last closed flux surface provides isolation between the plasma and the first wall. The distance $x_{\rm m}$ can be as small as 5 cm because (1) a 1-cm thickness is sufficient for the first wall (which supports only atmospheric loads and weak eddy-current loads); (2) the cryostat thickness can be only 2 cm because superinsulation is needed only on the outside of a polished liquid nitrogen shield; and (3) the plasma-facing coil case can be only 1.5 cm thick (zero in ATF) because it is only a winding form and experiences no inward force. An assembly gap of 0.5 cm is also assumed. The plasma-wall distance of 15 cm is very generous, so there is additional margin to relax constraints on the distance between the first wall and the HF winding pack or the thickness of the winding pack, if needed. The distance $c = (R_0 B_0/8MKj)^{1/2}$ can be reduced by elongating the winding cross section transverse to the radial depth ($K > 1$, where K is the ratio of the transverse width of the HF winding to its radial depth) and by increasing the average current density j in the winding pack subject to the $B_{\rm max}$ (j) constraint on the NbTi superconductor.

The principal constraints on B_0 and R_0 are plotted in Fig. 13 for a CT6 example. The geometrical constraint, the need for the space Δ between the edge of the plasma

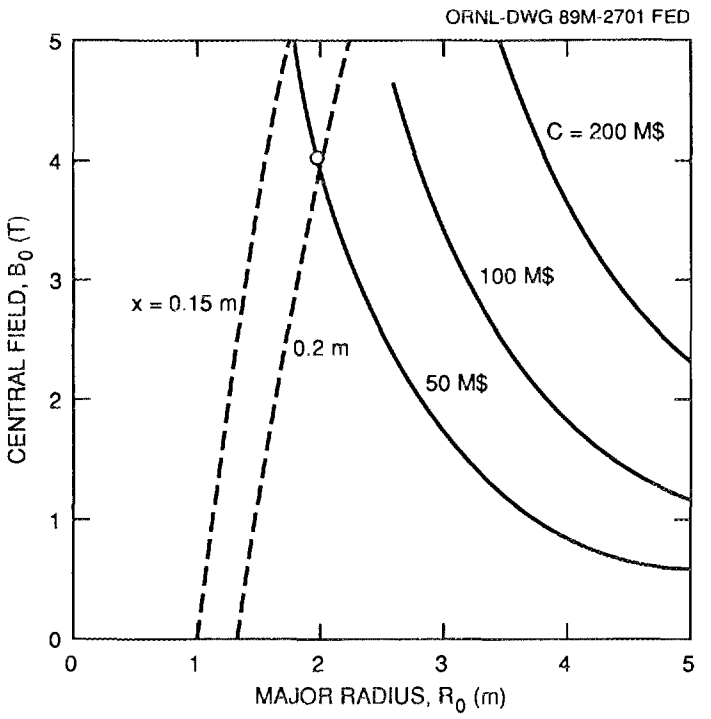

Fig. 13. Constraints imposed on B_0 vs R_0 for a CT6 ATF-II by geometry and the maximum field on the superconductor and by cost.

and the center of the HF winding, can be expressed as

$$B_0 = 8MKj(R_0/A_\Delta - x)^2/R_0 \ , \tag{2}$$

where $x = x_{\rm pw} + x_{\rm m}$ is the fixed (independent of B_0 and R_0) distance between the plasma edge and the surface of the HF winding pack. The maximum field $B_{\rm max}$ on the superconductor is obtained with the finite-element magnetic field code MAGFOR using the actual conductor cross section and the modulated helical winding trajectory. A close approximation is given by

$$B_0 = 0.029M(K+1)^2 B_{\rm max}^2/(KjR_0) \ . \tag{3}$$

Combining Eqs. (2) and (3) with the j-$B_{\rm max}$ relation for NbTi cable-in-conduit superconductor, which can be approximated by $j = 44.3 - 4.24B_{\rm max}$ at 4.2 K, gives the dashed curves ($x = 0.15$ m and 0.2 m) in Fig. 13.

The cost constraints (the solid curves in Fig. 13), which assume $j = 5$ kA/cm^2 and are valid over the cost range $C = \$30$ million to \$300 million, are given by

$$B_0 = 0.052M^{1.06}R^{-2.11}C \ . \tag{4}$$

The $B_0 = 4$ T, $R_0 = 2$ m configuration assumed for ATF-II is close to the $x = 0.2$ m, $C = \$50$ million intersection in Fig. 13.

The cost estimate in Eq. (4) fits within 10% the cost data derived from estimating[8] the base device costs for a large number of low-A torsatrons with different values of R_0, B_0, and M. The costs are calculated from the weights of each component, the cost per unit weight for machined material, a complexity factor derived from benchmarking component costs with those of ATF[23] and the comparisons in the ATF copper-coil vs superconducting-coil trade studies,[24] and the appropriate power supply costs or refrigeration costs. Plasma heating systems, diagnostics, site preparation, and other costs that are less dependent on the device scope are not included. The resulting cost coefficients used in the ATF-II studies are 2.1×10^5 \$/m^2 for the first wall, 5×10^4 \$/m^2 for the vacuum vessel, 2.5×10^{-3} \$/(A·m·T) for the superconductor, 250 \$/kg for the winding, 150 \$/kg for the winding case, 63 \$/kg for the dewar vessel, and 2.5×10^3 \$/m^2 for the superinsulation. Obviously, these rough values must be refined as better costing data become available from the LHD and W VII-X studies. Nevertheless, they have been used to define a target cost range for the ATF-II device of \$50 million to \$100 million.

The large distance between the HF windings for CT6 allows a large value for K, even on the small-R side. However, Table B.I in Appendix B shows that the plasma-wall separation increases slowly for $K > 2$, so extreme elongations are not necessary. We adopt the modest value $K = 2$, which gives $j_{\max} = 7.4$ kA/cm^2, $B_{\max} = 8.7$ T, a radial winding depth of 21 cm, and a minimum plasma-wall separation of 15 cm at 4.2 K. Dropping the helium temperature to 2.5 K for the same HF winding allows raising j to 9.3 kA/cm^2, $B_{\max}$ to 11 T, and B_0 to 5 T, so this coil design also allows 5-T operation of ATF-II with the same stability margin (100 mJ/cm^3) as for $B_0 = 4$ T at 4.2 K. The maximum quench pressure increases to 400 atm at 2.5 K, vs 210 atm at 4.2 K, but this is still well within our 500-atm constraint.

Table I shows the reference set of device parameters for ATF-II and a comparison with the $M = 12$ ATF. An $M = 6$ ATF-II could occupy roughly the same space as ATF. Its major radius is 5% smaller than that of ATF, and the outer diameter of its vacuum vessel is only 13% larger. However, ATF-II would have 1.9 times the plasma radius and 3.5 times the plasma volume of ATF, and the large outer ports (2.1 m^2) would have 3.9 times the area of those on ATF. In addition, the 4-T magnetic field would be twice that of ATF and would be steady state, compared with a 5-s limit at the maximum field of 2 T for the copper-coil ATF.

For the same plasma radius (and coincidentally the same cost[8]), an $M = 9$ ATF-II would be considerably larger ($R_0 = 2.4$ m). The larger outer diameter (6.8 m) of the vacuum vessel would make it difficult to locate on the ATF site. Reducing the outer diameter to be the same as an $M = 6$ ATF-II would decrease the plasma radius from 0.52 m to 0.46 m and the plasma volume from 12.6 m^3 to 9 m^3.

The relatively large plasma-wall distance in ATF-II ($\gtrsim$15 cm) and the large access ports allow use of the highly concentrated helical stripes of the diverted flux layer for particle collection and heat removal. Pumped particle collection ducts can be placed between the plasma edge and the wall if proximity to the last closed flux surface is important. Otherwise, the corners of the large outside horizontal ports (2.1 m $\times$ 1.0 m) or the top and bottom ports (2.0 m $\times$ 0.6 m) can be used as baffled pumping regions. The concept that would be used in ATF-II will arise from studies under way on ATF and Heliotron E and from the LHD design effort.

Table I. Comparison of ATF-II with ATF

	ATF-II	ATF
PLASMA		
Major radius (m)	2.0	2.1
Average radius (m)	0.52	0.27
Plasma volume (m^3)	10.6	3
Field on axis (T)	4 (5)[a]	2
HF WINDING		
Number of periods	6	12
Radius (m)	0.80	0.48
Length (m)	2 × 16	—
Current (MA-turns)	6.67 (8.33)	1.75
Coil cross section (m × m)	0.28 × 0.49	0.26 × 0.31
HF winding current density (kA/cm^2)	7.4 (9.3)	1.6
Maximum magnetic field on coil (T)	8.7 (11.0)	—
Maximum force (MN/m)	15.7 (24.8)	1.4
VACUUM VESSEL		
Outside diameter (m)	6.1	5.4
Inside (hole) diameter (m)	1.9	3
Height (m)	2.9	1.2
First wall i.d.: minimum, maximum (m)	1.1, 2.1	0.65, 1.2
Outside ports (m × m)	2.1 × 1.0	0.9 × 0.6
Top/bottom ports (m × m)	2.0 × 0.6	0.35 × 0.35
Inside ports (diameter, m)	—	0.2

[a] Values in parentheses are for operation with helium at 2.5 K, rather than the nominal 4.2 K.

VI. PERFORMANCE PROJECTIONS

Considering our state of ignorance on transport at high beta and/or low collisionality in large stellarators with optimized magnetic configurations, it is difficult to project the performance expected in ATF-II. This is, in fact, a major reason for experiments in ATF and for building ATF-II. Some rough estimates can be obtained from a simple scaling model, the LHD scaling[7] based primarily on the Heliotron E experiment, given by

$$\tau_E = 0.17 P^{-0.58} \bar{n}_e^{0.69} B_0^{0.84} \bar{a}^{2.0} R_0^{0.75} \quad . \tag{5}$$

(Here τ_E is in seconds, P in megawatts, B_0 in tesla, and $\bar{a}$ and R_0 in meters; $\bar{n}_e$ is in number of particles × 10^{20} m^3.) For an ATF-II with $B_0 = 4$ T, $\bar{a} = 0.52$ m, and $R_0 = 2$ m, this gives $\tau_E = 0.25 P^{-0.58} (\bar{n}_e)^{0.69}$. The highest value of τ_E is obtained for the highest density and the lowest heating power. For nominal values of $\bar{n}_e = 1 \times 10^{20}$ m^{-3} and $P = 10$ MW, $\tau_E = 65$ ms. Other quantities of interest ($n_0 \tau_E, T_0, \langle\beta\rangle$, and β_0, where T is the average of the electron and ion temperatures

and the subscript zero refers to the central value) can be obtained from Eq. (5) and standard definitions. Sudo et al.[7] propose in addition a density limit scaling,

$$\bar{n}_{e,max} = 0.25(PB_0/R_0\bar{a}^2)^{1/2} \quad . \tag{6}$$

If this density is used in Eq. (5), then

$$\tau_E = 0.065P^{-0.24}B_0^{1.19}\bar{a}^{1.31}R_0^{0.41} \quad . \tag{7}$$

The values of some quantities of interest for ATF-II are listed in Table II, with $P = 10$ MW and parabolic profiles for density and temperature assumed. For more peaked (parabolic-squared) profiles of density and temperature, these values are multiplied by 1.25 for $n_0\tau_E$, 1.33 for T_0, and 1.67 for β_0.

Table II. ATF-II Plasma Parameters from LHD Scaling

$\bar{n}_e$ (10^{20} m^{-3})	τ_E (ms)	$n_0\tau_E$ (10^{19} m^{-3}s)	T_0 (keV)	$\langle\beta\rangle$ (%)	β_0 (%)
0.25	25	0.094	3.91	0.25	0.74
0.5	40	0.30	3.16	0.40	1.19
1.0	65	0.98	2.55	0.64	1.92
2.15	110	3.55	2.01	1.08	3.25

The case with $\bar{n}_e = 2.15 \times 10^{20}$ m^{-3} in Table II represents the nominal density limit obtained from Eq. (6). The highest values are obtained at the highest density, except for the central temperature T_0, which is larger at lower densities. Higher values of beta can be obtained at lower field; at $B = 1$ T, $\bar{n}_{e,max} = 1.08 \times 10^{20}$ m^{-3}, $\tau_E = 21$ ms, $T_0 = 0.78$ keV, $\langle\beta\rangle = 3.4\%$, and $\beta_0 = 10.1\%$. Operation at higher field (5 T) in ATF-II would increase these values: at $\bar{n}_{e,max} = 2.4 \times 10^{20}$ m^{-3}, $\tau_E = 144$ ms, $n_0\tau_E = 5.2 \times 10^{19}$ m^{-3}·s, $T_0 = 2.34$ keV, $\langle\beta\rangle = 0.9\%$, and $\beta_0 = 2.7\%$.

These estimates of plasma parameters for ATF-II are close to those calculated for the other next-generation experiments, but they should not be taken too seriously. The scaling expressions in Eqs. (5)–(7) have not been verified at higher parameters, and a number of effects could improve confinement: profile shaping, positive radial electric fields, reduction of anomalous transport in the second stability regime, reduction of field errors, poloidal field shaping, plasma edge control, etc. A factor of two improvement in the τ_E given by Eq. (5) (and hence in T_0 and $\langle\beta\rangle$) would be more than sufficient to produce reactor-relevant parameters in ATF-II [$\tau_E = 0.22$ s, $T_0 = 7.8$–10.4 keV, $\langle\beta\rangle = 7\%$, $n_0\tau_E = (7.1$–$8.9) \times 10^{19}$ m^{-3}·s]. One-dimensional transport code calculations that incorporate some of these factors lead to more optimistic projections than this, but the calculations are sensitive to the assumptions on the radial electric field and the density profile near the edge[20] and must be tested by experiment.

VII. CONCLUSIONS

The ATF-II design scoping studies aim at producing a magnetic configuration with high beta and confinement properties at least as good as those projected for ATF, but at half the aspect ratio of ATF, in a coil configuration that would be attractive for a reactor. The most developed option for ATF-II, an $M = 6$ Compact Torsatron, satisfies most of these considerations and may be satisfactory for a next-generation experiment, but it would be useful to improve its confinement properties. An integrated optimization approach has yielded configurations with better confinement properties at high beta than projected for ATF or the Compact Torsatrons, but an attractive coil set to create these configurations needs to be developed. High-current-density, high-field, cable-in-conduit NbTi/Cu superconductor allows adequate plasma-wall separation (>15 cm) for a CT6 ATF-II with $R_0 = 2$ m and operation at $B = 4$ T with 4.2 K helium cooling or $B = 5$ T with 2.5 K helium cooling.

Considerable work remains before we have a fully satisfactory concept for ATF-II. Ripple-induced diffusive losses and energetic orbit losses at finite beta are a serious concern for ATF-II. Reducing these losses by using poloidal field coil sets and by pursuing alternative magnetic configurations is being investigated in our integrated optimization studies. Alternative configurations have not been refined to the point where attractive coil configurations can be specified. Work will continue on improving their confinement properties, developing quasi-helical coil configurations with good radial access, and increasing the plasma-wall distance for the modular variants. CT9, with a single helical winding and slightly larger plasma aspect ratio, $R_0/\bar{a} = 4.7$, is also being studied as a possible alternative to the base CT6 choice to understand the trade-offs between the CT9 and CT6 cases.

APPENDICES

A. INTEGRATED OPTIMIZATION STUDIES

The optimization approach used in determining the Compact Torsatron sequence started with the multiparameter specification for the helical winding trajectory given in Eq. (1) and varied the α_n parameters to maximize $\iota(\bar{a})$ subject to the constraints $\iota(0) \simeq 0.3$ and $V''(0) < 0$ (a central magnetic well). This approach had the advantage that the current windings needed to create the magnetic configuration were *a priori* known and geometrically simple. The disadvantage was that, with such a restricted set of external current windings, a large class of magnetic configurations was excluded from the optimization procedure. The integrated optimization procedure allows a much larger class of magnetic configurations (restricted only by the parametric form of the plasma boundary) because it makes no *a priori* assumptions about the currents that create them. However, there is no *a priori* reason to expect that the resulting winding geometry will be attractive for a low-aspect-ratio next-generation experiment or reactor. Nevertheless, the additional flexibility introduced by this procedure is useful for exploring the possible existence of configurations with improved confinement properties.

The conflicting requirements of MHD optimization and confinement optimization have led us to adopt the Garching optimization procedure[25] used in the VII-X studies, modified for low aspect ratio and different optimization criteria. Compact Torsatrons have more than adequate beta limits but reduced confinement properties at finite beta. We would be willing to trade somewhat reduced beta limits ($\langle\beta\rangle \sim 5\%$) for a factor of $\sim$3 improvement in confinement ($\sim$5–10% loss of energetic particles). The much larger improvements in confinement that can be obtained in quasi-helically symmetric systems at large aspect ratio are not necessary for ATF-II, and the resulting minimization of magnetic axis shift with increasing beta is not compatible with the beta self-stabilization effect that produces a second stability regime at low aspect ratio.

The integrated optimization approach uses a multiparameter characterization of the plasma boundary, a three-dimensional (3-D) plasma equilibrium code (VMEC[26]), and a multidimensional nonlinear optimization routine[27] to find the finite-beta magnetic configuration that best satisfies the imposed stability and confinement criteria.[28] The Fourier harmonic expansion of the plasma boundary (last closed flux surface) is given by[29]

$$R = \sum_{n=0}^{N} R_{0n} \cos n\phi + \sum_{n=-N}^{N} R_{1n} \cos(\theta - n\phi) + \bar{r} \cos\theta \ ,$$

$$Z = \sum_{n=0}^{N} Z_{0n} \sin n\phi - \sum_{n=-N}^{N} R_{1n} \sin(\theta - n\phi) + \bar{r} \sin\theta \ , \qquad \text{(A.1)}$$

$$\bar{r} = \sum_{n=0}^{N} r_{0n} \cos n\phi + \sum_{n=-N}^{N} r_{3n} \cos(3\theta - n\phi) \ .$$

Seven of the coefficients are allowed to vary during the course of the optimization: R_{0M}, Z_{0M}, R_{10}, R_{1M}, r_{30}, r_{0M}, and r_{3M}, with $r_{00} = 1 - R_{1M}$ to keep the aspect ratio fixed during the iterations. The other coefficients are zero. Starting from an initial trial plasma boundary, which entirely determines the plasma properties, small variations of the parametrization of the plasma boundary produce nonlinear incremental changes in the MHD and confinement properties of the plasma. Numerical calculation of these changes allows a systematic selection of nearby configurations in the multi-dimensional boundary-parameter space until the best solution is found. The number of field periods, M, remains fixed during the course of the optimization.

The optimization criteria used are the deviation from target values of edge and central transform (approximately those of ATF to allow moderate values of transform and shear and to avoid the most dangerous low-order rational values of ι), the percentage of the plasma that is Mercier unstable, and the percentage of the plasma in which deeply trapped particles are confined. We exclude the region $\psi < 0.2$, where ψ is the normalized toroidal flux, from evaluation of the Mercier criterion[13] to avoid inherent numerical problems with evaluation of currents near the magnetic axis. This procedure is more effective than maximizing the radial extent of the central magnetic well and minimizing the value of the magnetic hill at the plasma edge. Confinement is improved by maximizing the midplane width of the last $B_{\min}$ contour to close in the plasma and by minimizing the distance between the center of this contour and the magnetic axis. These criteria are found to correlate well with the fraction of trapped particles lost in the full 3-D energetic orbit calculations.[28]

The optimization criteria are combined in a figure of merit F that is minimized:

$$F = x_{\mathrm{a}} \tanh(\gamma x_{\mathrm{a}}) + x_{\mathrm{e}} \tanh(\gamma x_{\mathrm{e}}) + \alpha L_{\mathrm{M}} - \delta L_{\mathrm{B}} ,$$

$$x_{\mathrm{a}} = (\iota_{\mathrm{a}} - \iota_{\mathrm{a0}})/\iota_{\mathrm{a0}}, \; x_{\mathrm{e}} = (\iota_{\mathrm{e}} - \iota_{\mathrm{e0}})/\iota_{\mathrm{e0}} , \tag{A.2}$$

where ι_{a} and ι_{e} are the computed rotational transform at the magnetic axis and plasma edge, respectively, and ι_{a0} and ι_{e0} are the corresponding desired transform values; L_{M} is the percentage of the plasma that is Mercier unstable; L_B is the percentage width of the last closed $B_{\min}$ contour; and α, γ, and δ are constants chosen to steer the optimization in the desired direction. The tanh functions in Eq. (A.2) prevent the optimization function from increasing too rapidly when the transform values differ greatly from their target values while providing a sum of squares behavior near the optimum. Experience has shown that this form provides the most reliable results.[27] Typical values for the constants γ, α, and δ are $\gamma = 10$, $\alpha = 20$–30, and $\delta = 2$–3.

B. SUPERCONDUCTING WINDING OPTIMIZATION

High-current-density, high-field, stable superconducting windings are feasible with existing NbTi conductor technology.[30] In tests at Oak Ridge National Laboratory,[31,32] forced-flow, cable-in-conduit superconductor wound into a coil was operated at 7.7 T (at 4.2 K) with a current density of 6.4 kA/cm^2 averaged over

the winding with a stability margin of 30–40 mJ/cm^3, excellent insulation and structural integrity, and no "training period" required. At $B = 7$ T, reducing the temperature from above 3.8 K to below 3.7 K increased the stability margin from 50 mJ/cm^3 to $\simeq$180 mJ/cm^3. Results from the Large Coil Task (LCT) indicate that a stability margin of 100 mJ/cm^3 is sufficient to handle the perturbations that occur from the electromagnetic forces.[33] The stability margin adopted is 25 times that of the successful 8-T, 10-kA/cm^2 coil developed for the ELMO Bumpy Torus Proof-of-Principle experiment and twice that of the Euratom LCT coil, neither of which has ever (unintentionally) gone normal. The equivalent values of j obtained in other magnets are considerably lower: 1.5–1.8 kA/cm^2 at 8 T and 4 K in the LCT NbTi magnets and 5 kA/cm^2 at 9 T and 1.8 K in the Tore Supra magnets (which, however, are not cryostable). More tests are required to select the conductor design most compatible with the stability, quench protection, and thermal performance needs of the ATF-II coils.

Force-flow (FF) cooling of the superconductor has a number of advantages. High-voltage integrity (2–10 kV) can be maintained by fully wrapping the conduit with multiple layers of insulation. The forces can be transmitted to the external case by potting the windings in a low-temperature epoxy. Any design with adequate structure can be extrapolated to higher field by lowering the operating temperature below 4.2 K, because the heat transfer is not degraded as the temperature is lowered. Forces and stresses on potted FF-cooled magnets can be calculated with higher reliability than those on pool-boiling (PB) magnets. A resulting advantage of this approach is that prototype magnet testing is not required, and the results from tests of a relatively small-scale model magnet can be extrapolated to a full-size system. This would reduce the cost and the time needed for the research and development program for the ATF-II coils.

In a cable-in-conduit conductor, the superconductor is contained in a braided cable that is enclosed in a protective jacket. Cooling is provided by pressurized (15-atm) helium that remains single phase. Three candidate conductor designs for ATF-II are shown in Fig. B.1. Helium, usually supercritical (but possibly superfluid), fills the interstices of the cable. The strands that make up the cable

ORNL-DWG 89M-2671A FED

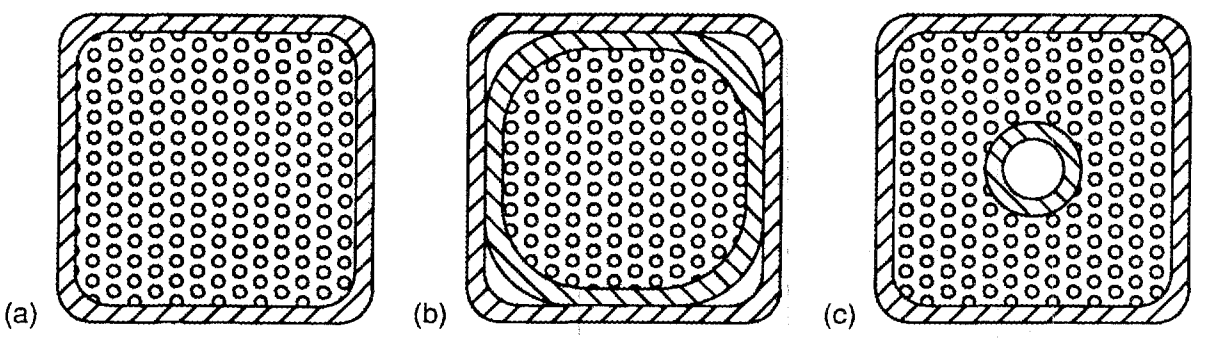

Fig. B.1. Three candidates for ATF-II force-flow cable-in-conduit conductor: (a) plain cable in conduit, (b) cable in double conduit, and (c) tube in cable in conduit.

are composed of a matrix material (usually copper, but possibly aluminum) in which many fine filaments of NbTi superconductor are embedded. Because of the small diameter of the strands in the cable, the metal strands have a large surface wetted by the helium. When any heat is generated internally, the increased pressure leads to induced flow of supercritical helium (enhanced by the tight confinement of the helium in the cable), providing additional heat transfer to guarantee recovery. Heat generated externally (e.g., frictional motion) is intercepted by the helium and never affects the superconductor. The resulting excellent heat transfer results in a high stability margin (>100 mJ/cm^3) and allows cable-in-conduit conductors to operate stably at higher current densities than is possible with monolithic PB-cooled conductors.

Calculations have been made of the variation of the maximum quench pressure and the stability margin with the fraction of the conductor cross section that is copper and the fraction of the conductor area over the cable space.[30,34,35] A stability margin of more than 100 mJ/cm^3 can readily be obtained at $B = 8$ T for a cable space (copper, NbTi superconductor, helium) current density j_{cs} of 20 kA/cm^2 (corresponding to a total winding pack current density j of 12 kA/cm^2) with a 20–25% void fraction and a copper-to-superconductor ratio of 2–3 at 4 K. Stable conductor performance at even higher current density ($j_{cs} = 30$ kA/cm^2, $j = 18$ kA/cm^2) at $B = 10$ T can be obtained if superfluid He II at 1.8 K is used for the coolant.

Specifications for the superconductor in the HF windings can be obtained from calculations of the type described above. Assuming a 100-mJ/cm^3 stability margin and $\leq$500-atm quench pressure gives the j-B_{max} relation (the solid curves) shown in Fig. B.2. A large increase in j can be obtained, especially at higher field, by lowering the helium temperature. The other relation between j and B_{max} (the dashed curves in Fig. B.2) involving the transverse elongation K of the winding cross section results from the CT6 HF coil geometry [see Eq. (3)]. The intersection of these curves gives the maximum value of j ($= j_{max}$) allowed for a given K that satisfies the j-B_{max} conductor constraint. Table B.I gives the variation of j_{max} and B_{max} with K and the resulting variation of radial winding depth ($2c$) and minimum plasma-wall separation (x_{pw}) with K for the CT6 case. These calculations suggest that a reasonable target for an ATF-II winding with a stability margin of 100 mJ/cm^3 is $j = 7.4$ kA/cm^2 and $B_{max} = 8.7$ T at 4.2 K or $j = 11$ kA/cm^2 and $B_{max} = 10.6$ T at 2.5 K, corresponding to $K = 2$. Although there is a large variation in j_{max} and B_{max} with helium temperature, the variation in winding depth and plasma-wall separation is much smaller because $c \propto (Kj_{max})^{-1/2}$. Thus, it is not necessary to go to 1.8 K and superfluid helium to obtain more than adequate plasma-wall spacing. We adopt 4.2 K as our usual operating temperature. This allows us to go to 2.5 K if we wish to increase the field to 5 T with the same conductor.

The most likely limiting factor for high-current-density, cable-in-conduit conductors is the quench pressure. The maximum allowable internal pressure depends on the jacket thickness and the winding pack structure. We assume a maximum allowed quench pressure of 500 atm (vs 800 atm for the International Thermonuclear Experimental Reactor) for $T = 4.2$ K to 2.5 K. The maximum quench pressure is not an issue for 1.8 K operation because the superfluid He II would not need to be tightly

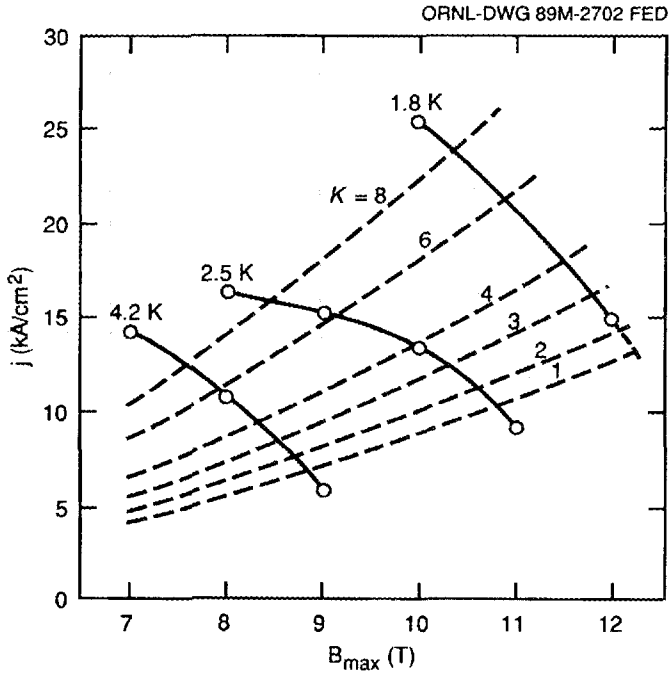

Fig. B.2. Constraints on the average HF winding current density j vs the maximum field B_{max} in the ATF-II NbTi/Cu cable-in-conduit conductor from the winding geometry (dashed lines for constant winding elongation K) and from the maximum allowed quench pressure and the desired stability margin (solid curves for constant helium temperature).

Table B.I. Variation of HF Winding Parameters with K

		K				
Parameter	T (K)	1	2	3	4	6
j_{max} (kA/cm)	4.2	6.8	7.4	8.4	9.4	11.0
	2.5	10.2	11.0	12.3	13.4	14.8
	1.8	13.1	14.2	16.1	18.0	21.1
B_{max} (T)	4.2	8.9	8.7	8.6	8.3	7.9
	2.5	10.8	10.6	10.3	9.9	9.2
	1.8	12.2	12.1	11.8	11.5	10.9
Coil depth (cm)	4.2	31.3	21.2	16.3	13.3	10.0
	2.5	25.6	17.4	13.4	11.2	8.7
	1.8	22.6	15.3	11.7	9.6	7.3
Minimum plasma-	4.2	9.6	14.6	17.1	18.6	20.2
wall distance	2.5	12.4	16.5	18.5	19.6	20.9
x_{pw} (cm)	1.8	13.9	17.5	19.3	20.4	21.6

contained in the inner conduit. Limited data on quench propagation are available for the Westinghouse LCT coil, and analytic calculations[36] exist on hot/cold front propagation, pressure rise, helium expulsion velocity, and normal zone propagation along the conductor. These calculations show that if the whole 20-m hydraulic path goes normal, hot/cold front propagation and helium expulsion velocities of $\simeq$50 m/s and a pressure rise of $\simeq$90 atm can be expected. For a shorter heated zone, the velocities and pressure decrease. Our design allows a maximum quench pressure of 500 atm. An experiment is needed to answer the major remaining issues on quench propagation: the effects of the additional copper of the inner conduit; the effect on the helium warm-front velocity and thermal expulsion of the larger flow channels at the corners (Fig. B.1b); and the reduction of the maximum quench pressure due to the expulsion of helium.

REFERENCES

1. B.A. CARRERAS, G. GRIEGER, J.H. HARRIS, J. L. JOHNSON, J.F. LYON, O. MOTOJIMA, et al., "Progress in Stellarator/Heliotron Research: 1981–1986," *Nucl. Fusion*, **28**, 1613 (1988).
2. J.F. LYON, "Near-Term Directions in the World Stellarator Program," *Fusion Technol.*, accepted for publication (1989).
3. DESIGN GROUP FOR THE NEW LARGE HELICAL SYSTEM DEVICE, "New Large Helical System Device—Outline," unpublished (1988); see also A. IIYOSHI and the LHD DESIGN TEAM, "Design Study of the Large Helical Device," *Fusion Technol.*, accepted for publication (1989).
4. F. RAU and G.G. LEOTTA, Eds., *Proc. 2nd Workshop on Wendelstein VII-X,* Schloss Ringberg, Federal Republic of Germany, 1988, EUR 11705 EN, Commission of the European Communities, Brussels (1988); see also C. BEIDLER, G. GRIEGER, F. HERRNEGGER, E. HARMEYER, J. KISSLINGER, H. MAASSBERG, et al., "Physics and Engineering Design for Wendelstein VII-X," *Fusion Technol.*, accepted for publication (1989).
5. B.A. CARRERAS, "Low-Aspect-Ratio Torsatrons," *Comments Plasma Phys. Controlled Fusion*, **11**, 139 (1987).
6. J.F. LYON, B.A. CARRERAS, K.K. CHIPLEY, M.J. COLE, J.H. HARRIS, et al., "The Advanced Toroidal Facility," *Fusion Technol.*, **10**, 179 (1986).
7. S. SUDO, Y. TAKEIRI, H. ZUSHI, F. SANO, K. ITOH, K. KONDO, and A. IIYOSHI, "Scalings of Energy Confinement and Density Limit in Stellarator/Heliotron," submitted to *Nucl. Fusion* (1989); see also PPLK-R-40, Kyoto University (1989).
8. B.A. CARRERAS, R.H. FOWLER, V.E. LYNCH, J.F. LYON, and S.L. PAINTER, "Fusion Energy Division Annual Progress Report for Period Ending December 31, 1987," ORNL-6452, Sec. 1.2.1, Oak Ridge National Laboratory (1988).
9. B.A. CARRERAS, N. DOMINGUEZ, L. GARCIA, V.E. LYNCH, J.F. LYON, et al., "Low-Aspect-Ratio Torsatron Configurations," *Nucl. Fusion*, **28**, 1195 (1988).
10. B.A. CARRERAS, V.E. LYNCH, N. DOMINGUEZ, J.N. LEBOEUF, and J.F. LYON, "Confinement Improvement of Low-Aspect-Ratio Torsatrons," ORNL/TM-11101, Oak Ridge National Laboratory (1989).
11. J.R. CARY and J.D. HANSON, "Stochasticity Reduction," *Phys. Fluids*, **29**, 2464 (1986).
12. L.M. KOVRIZHNYKH and S.V. SHCHEPETOV, "Self-Stabilization of a Finite-β Plasma in a Stellarator," *Sov. J. Plasma Phys.*, **7**, 229 (1981) [*Fiz. Plazmy*, **7**, 419 (1981)].
13. C. MERCIER, "Un Critere Necessaire de Stabilité Hydromagnetique pour un Plasma en Symetrie de Revolution," *Nucl. Fusion*, **1**, 47 (1960).
14. K.C. SHAING, B.A. CARRERAS, N. DOMINGUEZ, V.E. LYNCH, and J.S. TOLLIVER, "Bootstrap Current Control in Stellarators," *Phys. Fluids B*, **1**, 1663 (1989).

15. S.L. PAINTER and J.F. LYON, "Alpha-Particle Losses in Compact Torsatron Reactors," *Fusion Technol.*, **16**, 157 (1989); see also ORNL/TM-10792, Oak Ridge National Laboratory (1988).
16. B.A. CARRERAS, N. DOMINGUEZ, L. GARCIA, J.F. LYON, S.L. PAINTER, J. SHEFFIELD, V.E. LYNCH, J.R. CARY, and J.D. HANSON, "Low-Aspect-Ratio Torsatrons," *Proc. 12th Int. Conf. Plasma Phys. Controlled Nuclear Fusion Research*, Nice, France, 1988, IAEA-CN-50/C-I-5-2, to be published by the International Atomic Energy Agency, Vienna (1989).
17. V.A. BATYUK, G.S. VORONOV, E.F. GIPPIUS, S.E. GREBENSHCHIKOV, N.P. DONSKAYA, K.S. KYABILIN, et al., "Plasma Heating at the Fundamental Ion Cyclotron Frequency in the L-2 Stellarator," *Sov. J. Plasma Phys.*, **13**, 143 (1987) [*Fiz. Plazmy*, **13**, 259 (1987)].
18. K.C. SHAING and S.A. HOKIN, "Neoclassical Transport in a Multiple Helicity Torsatron in the Low Collisionality ($1/\nu$) Regime," *Phys. Fluids*, **26**, 2136 (1983).
19. B.A. CARRERAS, "Anomalous Transport in the Second Stability Regime," *Comments Plasma Phys. Controlled Fusion*, **12**, 35 (1988).
20. J.F. LYON, B.A. CARRERAS, V.E. LYNCH, J.S. TOLLIVER, and I.N. SVIATOSLAVSKY, "Compact Torsatron Reactors," *Fusion Technol.*, **15**, 1401 (1989).
21. JAMES ROME, ROBERT MORRIS, STEVEN HIRSHMAN, and RONALD FOWLER, "Coil Configurations for Low-Aspect-Ratio Stellarators," *Proc. 7th Int. Workshop on Stellarators*, Oak Ridge, Tennessee, 1989, to be published by the International Atomic Energy Agency, Vienna (1989).
22. P. MERKEL, "Solution of Stellarator Boundary Value Problems with External Currents," *Nucl. Fusion*, **27**, 867 (1987).
23. P.B. THOMPSON, Engineering Division, Martin Marietta Energy Systems, Inc., private communication (1988).
24. B.E. NELSON, Engineering Division, Martin Marietta Energy Systems, Inc., private communication (1982).
25. J. NÜHRENBERG and R. ZILLE, "Stable Stellarators with Medium β and Aspect Ratio," *Phys. Lett.*, **114A**, 129 (1986).
26. S.P. HIRSHMAN, U. SCHWENN, and J. NÜHRENBERG, "Improved Radial Dif- ferencing for Three-Dimensional Magnetohydrodynamic Equilibrium Calculations," *J. Comput. Phys.*, accepted for publication (1989).
27. R.N. MORRIS, C.L. HEDRICK, S.P. HIRSHMAN, J.F. LYON, and J.A. ROME, "Numerical Methods for Stellarator Optimization," *Proc. 7th Int. Workshop on Stellarators*, Oak Ridge, Tennessee, 1989, to be published by the International Atomic Energy Agency, Vienna (1989).
28. S.P. HIRSHMAN, R.N. MORRIS, C.L. HEDRICK, J.F. LYON, J.A. ROME, S.L. PAINTER, and W.I. VAN RIJ, "Low-Aspect-Ratio Optimization Studies for ATF-II," *Proc. 7th Int. Workshop on Stellarators*, Oak Ridge, Tennessee, 1989, to be published by the International Atomic Energy Agency, Vienna (1989).

29. S.P. HIRSHMAN and H. WEITZNER, "A Convergent Spectral Representation for Three-Dimensional Inverse Magnetohydrodynamic Equilibria," *Phys. Fluids*, **28**, 1207 (1985).
30. J.W. LUE, L. DRESNER, and M.S. LUBELL, "High-Field, High-Current-Density, Stable Superconducting Magnets for Fusion Machines," *Proc. 7th Int. Workshop on Stellarators*, Oak Ridge, Tennessee, 1989, to be published by the International Atomic Energy Agency, Vienna (1989).
31. J.R. MILLER, J.W. LUE, R.L. BROWN, and W.J. KENNEY, "Design, Construction, and Test of a 113-mm Bore Solenoid with NbTi Cable-in-Conduit Superconducting Windings," *IEEE Trans. Magn.*, **MAG-17**, 2250 (1981).
32. J.W. LUE and J.R. MILLER, "Performance of an Internally Cooled Superconducting Solenoid," *Adv. Cryog. Eng.*, **27**, 227 (1982).
33. D.S. BEARD, W. KLOSE, S. SHIMAMOTO, and G. VECSEY, eds., "The IEA Large Coil Task," *Fusion Eng. Des.*, **7**, 1–232 (1988).
34. J.W. LUE, J.R. MILLER, and L. DRESNER, "Stability of Cable-in-Conduit Superconductors," *J. Appl. Phys.*, **51**, 772 (1980).
35. L. DRESNER, "Parametric Study of the Stability Margin of Cable-in-Conduit Superconductors: Theory," *IEEE Trans. Magn.*, **MAG-17**, 757 (1981).
36. L. DRESNER, "Quench Pressure, Thermal Expulsion, and Normal Zone Propagation in Internally Cooled Superconductors," *IEEE Trans. Magn.*, **MAG-25**, 1710 (1989).

ORNL/TM-11254
Dist. Category UC-426

INTERNAL DISTRIBUTION

1. C. C. Baker
2. L. A. Berry
3. B. A. Carreras
4. N. Dominguez
5. R. A. Dory
6. L. Dresner
7. J. L. Dunlap
8. R. H. Fowler
9. W. Fulkerson
10. J. H. Harris
11. H. H. Haselton
12. C. L. Hedrick
13. S. P. Hirshman
14. J. T. Hogan
15. R. C. Isler
16. T. C. Jernigan
17. R. L. Johnson
18. M. S. Lubell
19. J. W. Lue
20. J. N. Luton
21–25. J. F. Lyon
26. P. K. Mioduszewski
27. R. N. Morris
28. M. Murakami
29. G. H. Neilson
30. B. E. Nelson
31. S. L. Painter
32. Y-K. M. Peng
33. J. A. Rome
34. M. J. Saltmarsh
35. T. E. Shannon
36. D. W. Swain
37. N. A. Uckan
38. W. I. van Rij
39. J. Sheffield
40–41. Laboratory Records Department
42. Laboratory Records, ORNL-RC
43. Central Research Library
44. Document Reference Section
45. Fusion Energy Division Library
46–47. Fusion Energy Division Publications Office
48. ORNL Patent Office

EXTERNAL DISTRIBUTION

49. Office of the Assistant Manager for Energy Research and Development, U.S. Department of Energy, Oak Ridge Operations Office, P. O. Box E, Oak Ridge, TN 37831
50. J. D. Callen, Department of Nuclear Engineering, University of Wisconsin, Madison, WI 53706-1687
51. R. W. Conn, Department of Chemical, Nuclear, and Thermal Engineering, University of California, Los Angeles, CA 90024
52. N. A. Davies, Acting Director, Office of Fusion Energy, Office of Energy Research, ER-50 Germantown, U.S. Department of Energy, Washington, DC 20545
53. S. O. Dean, Fusion Power Associates, Inc., 2 Professional Drive, Suite 248, Gaithersburg, MD 20879

54. H. K. Forsen, Bechtel Group, Inc., Research Engineering, P. O. Box 3965, San Francisco, CA 94119
55. J. R. Gilleland, L-644, Lawrence Livermore National Laboratory, P.O. Box 5511, Livermore, CA 94550
56. R. W. Gould, Department of Applied Physics, California Institute of Technology, Pasadena, CA 91125
57. R. A. Gross, Plasma Research Laboratory, Columbia University, New York, NY 10027
58. D. M. Meade, Princeton Plasma Physics Laboratory, P.O. Box 451, Princeton, NJ 08543
59. M. Roberts, International Programs, Office of Fusion Energy, Office of Energy Research, ER-52 Germantown, U.S. Department of Energy, Washington, DC 20545
60. W. M. Stacey, School of Nuclear Engineering and Health Physics, Georgia Institute of Technology, Atlanta, GA 30332
61. D. Steiner, Nuclear Engineering Department, NES Building, Tibbetts Avenue, Rensselaer Polytechnic Institute, Troy, NY 12181
62. R. Varma, Physical Research Laboratory, Navrangpura, Ahmedabad 380009, India
63. Bibliothek, Max-Planck Institut für Plasmaphysik, Boltzmannstrasse 2, D-8046 Garching, Federal Republic of Germany
64. Bibliothek, Institut für Plasmaphysik, KFA Jülich GmbH, Postfach 1913, D-5170 Jülich, Federal Republic of Germany
65. Bibliothek, KfK Karlsruhe GmbH, Postfach 3640, D-7500 Karlsruhe 1, Federal Republic of Germany
66. Bibliotheque, Centre de Recherches en Physique des Plasmas, Ecole Polytechnique Fédérale de Lausanne, 21 Avenue des Bains, CH-1007 Lausanne, Switzerland
67. R. Aymar, CEN/Cadarache, Departement de Recherches sur la Fusion Contrôlée, F-13108 Saint-Paul-lez-Durance Cedex, France
68. Bibliothèque, CEN/Cadarache, F-13108 Saint-Paul-lez-Durance Cedex, France
69. Library, Culham Laboratory, UKAEA, Abingdon, Oxfordshire, OX14 3DB, England
70. Library, JET Joint Undertaking, Abingdon, Oxfordshire OX14 3EA, England
71. Library, FOM-Instituut voor Plasmafysica, Rijnhuizen, Edisonbaan 14, 3439 MN Nieuwegein, The Netherlands
72. Library, National Institute for Fusion Science, Chikusa-ku, Nagoya 464-01, Japan
73. Library, International Centre for Theoretical Physics, P.O. Box 586, I-34100 Trieste, Italy
74. Library, Centro Richerche Energia Frascati, C.P. 65, I-00044 Frascati (Roma), Italy

75. Library, Plasma Physics Laboratory, Kyoto University, Gokasho, Uji, Kyoto 611, Japan
76. Plasma Research Laboratory, Australian National University, P.O. Box 4, Canberra, A.C.T. 2601, Australia
77. Library, Japan Atomic Energy Research Institute, Naka Fusion Research Establishment, 801-1 Mukoyama, Naka-machi, Naka-gun, Ibaraki-ken, Japan
78. G. A. Eliseev, I. V. Kurchatov Institute of Atomic Energy, P. O. Box 3402, 123182 Moscow, U.S.S.R.
79. V. A. Glukhikh, Scientific-Research Institute of Electro-Physical Apparatus, 188631 Leningrad, U.S.S.R.
80. I. Shpigel, Institute of General Physics, U.S.S.R. Academy of Sciences, Ulitsa Vavilova 38, Moscow, U.S.S.R.
81. D. D. Ryutov, Institute of Nuclear Physics, Siberian Branch of the Academy of Sciences of the U.S.S.R., Sovetskaya St. 5, 630090 Novosibirsk, U.S.S.R.
82. O. S. Pavlichenko, Kharkov Physical-Technical Institute, Academical St. 1, 310108 Kharkov, U.S.S.R.
83. Deputy Director, Southwestern Institute of Physics, P.O. Box 15, Leshan, Sichuan, China (PRC)
84. Director, The Institute of Plasma Physics, P.O. Box 26, Hefei, Anhui, China (PRC)
85. R. A. Blanken, Experimental Plasma Research Branch, Division of Applied Plasma Physics, Office of Fusion Energy, Office of Energy Research, ER-542, Germantown, U.S. Department of Energy, Washington, DC 20545
86. R. A. E. Bolton, IREQ Hydro-Quebec Research Institute, 1800 Montee Ste.-Julie, Varennes, P.Q. JOL 2P0, Canada
87. D. H. Crandall, Experimental Plasma Research Branch, Division of Applied Plasma Physics, Office of Fusion Energy, Office of Energy Research, ER-542, Germantown, U.S. Department of Energy, Washington, DC 20545
88. R. L. Freeman, General Atomics, P.O. Box 85608, San Diego, CA 92138-5608
89. K. W. Gentle, RLM 11.222, Institute for Fusion Studies, University of Texas, Austin, TX 78712
90. R. J. Goldston, Princeton Plasma Physics Laboratory, P.O. Box 451, Princeton, NJ 08543
91. J. C. Hosea, Princeton Plasma Physics Laboratory, P.O. Box 451, Princeton, NJ 08543
92. R. Dagazian, Division of Confinement Systems, Office of Fusion Energy, Office of Energy Research, ER-55, Germantown, U.S. Department of Energy, Washington, DC 20545
93. R. H. McKnight, Experimental Plasma Research Branch, Division of Applied Plasma Physics, Office of Fusion Energy, Office of Energy Research, ER-542, Germantown, U.S. Department of Energy, Washington, DC 20545

94. E. Oktay, Division of Confinement Systems, Office of Fusion Energy, Office of Energy Research, ER-55, Germantown, U.S. Department of Energy, Washington, DC 20545
95. D. Overskei, General Atomics, P.O. Box 85608, San Diego, CA 92138-5608
96. R. R. Parker, Plasma Fusion Center, NW 16-288, Massachusetts Institute of Technology, Cambridge, MA 02139
97. W. L. Sadowski, Fusion Theory and Computer Services Branch, Division of Applied Plasma Physics, Office of Fusion Energy, Office of Energy Research, ER-541, Germantown, U.S. Department of Energy, Washington, DC 20545
98. J. W. Willis, Division of Confinement Systems, Office of Fusion Energy, Office of Energy Research, ER-55, Germantown, U.S. Department of Energy, Washington, DC 20545
99. A. P. Navarro, Division de Fusion, CIEMAT, Avenida Complutense 22, E-28040 Madrid, Spain
100. Laboratory for Plasma and Fusion Studies, Department of Nuclear Engineering, Seoul National University, Shinrim-dong, Gwanak-ku, Seoul 151, Korea
101. J. L. Johnson, Plasma Physics Laboratory, Princeton University, P.O. Box 451, Princeton, NJ 08543
102. L. M. Kovrizhnykh, Institute of General Physics, U.S.S.R. Academy of Sciences, Ulitsa Vavilova 38, 117924 Moscow, U.S.S.R.
103. T. Obiki, Plasma Physics Laboratory, Kyoto University, Gokasho, Uji, Kyoto, Japan
104. A. Iiyoshi, National Institute for Fusion Science, Chikusa-ku, Nagoya 464-01, Japan
105. V. D. Shafranov, I. V. Kurchatov Institute of Atomic Energy, P.O. Box 3402, 123182 Moscow, U.S.S.R.
106. J. L. Shohet, Torsatron/Stellarator Laboratory, University of Wisconsin, Madison, WI 53706
107. G. Grieger, Max-Planck Institut fur Plasmaphysik, D-8046 Garching, Federal Republic of Germany
108. K. Matsuoka, National Institute for Fusion Science, Chikusa-ku, Nagoya 464-01, Japan
109. F. L. Ribe, University of Washington, Aerospace and Energetics Research Program, Mail Stop FL-10, Seattle, WA 98915
110. D. G. Swanson, Auburn University, Department of Physics, Auburn, AL 36849
111. R. K. Linford, Los Alamos National Laboratory, MS F646, P.O. Box 1663, Los Alamos, NM 87545
112. K. I. Thomassen, L-637, Lawrence Livermore National Laboratory, P.O. Box 5511, Livermore, CA 94550
113. R. F. Gandy, Physics Department, Auburn University, Auburn, AL 36849

114–164. Given distribution as shown in OSTI-4500, Magnetic Fusion Energy (Category Distribution UC-426)